



Synthesis of a graphene–tungsten composite with improved dispersibility of graphene in an ethanol solution and its use as a counter electrode for dye-sensitised solar cells

B. Munkhbayar^a, Md. J. Nine^a, Jinseong Jeoun^a, Myoungkuk Ji^b, Hyomin Jeong^c, Hanshik Chung^{c,*}

^aDepartment of Energy and Mechanical Engineering, Gyeongsang National University, 445 Inpyeongdong, Tongyeong 650-160, Gyeongnam, Republic of Korea

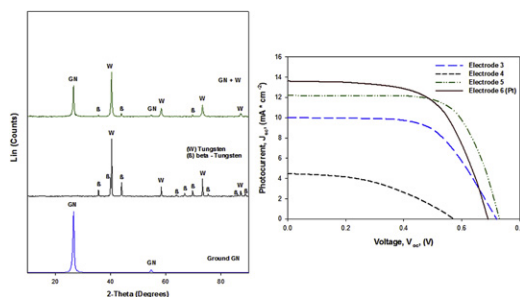
^bYoung Jin Forgin Co., Ltd., Republic of Korea

^cDepartment of Energy and Mechanical Engineering, Institute of Marine Industry, Gyeongsang National University, 445 Inpyeongdong, Tongyeong 650-160, Gyeongnam, Republic of Korea

HIGHLIGHTS

- Dispersibility of GN solution is improved by acid oxidation and grinding approaches.
- Photovoltaic performance of DSSC with GN was improved after planetary ball milling.
- DSSC with GN, tungsten and GN–tungsten composite counter electrodes are fabricated.
- DSSC with GN–tungsten composite counter electrode recorded an efficiency of 5.88%.
- GN–tungsten composite can be potential material for replacing expensive Pt in DSSC.

GRAPHICAL ABSTRACT



ARTICLE INFO

Article history:

Received 31 October 2012

Received in revised form

12 December 2012

Accepted 15 December 2012

Available online 22 December 2012

Keywords:

Dye-sensitised solar cell

Counter electrode

Graphene

Tungsten

Dispersibility

ABSTRACT

The article reports a nanocomposite (graphene and tungsten (GN–W)) successfully used as an alternative to a conventional Pt counter electrode in dye-sensitised solar cells (DSSCs). The dispersibility of the GN structure in ethanol was enhanced by acid oxidation and planetary ball milling. Raw, purified and purified and ground GN structures were spin coated onto fluorine-doped tin oxide (FTO) glass substrates and examined as catalytic films on the counter electrodes of DSSCs. Purified and ground GNs exhibited the best photovoltaic performance (4.55%) among these structures. The grinding method was found effective for upgrading the dispersibility of GNs in a base fluid and the photovoltaic efficiency results. Based on the photovoltaic efficiency results of the DSSCs with different GN structures, the purified and ground GN structure was selected and incorporated with tungsten. A composite film of GN–W was used as a catalytic film on the counter electrode of a DSSC. The DSSC fabricated with the GN–W composite counter electrode achieved a photovoltaic efficiency of 5.88%. This performance is comparable to that of a DSSC with a standard Pt counter electrode (5.92%).

© 2012 Elsevier B.V. All rights reserved.

1. Introduction

As a third-generation photovoltaic device, DSSCs have gained considerable attention in recent years because of their high

* Corresponding author. Tel./fax: +82 (0)55 772 9115.

E-mail addresses: muugii_3685@yahoo.com (B. Munkhbayar), hschung@gnu.ac.kr (H. Chung).

efficiency, low cost, environmental friendliness, and easy fabrication [1–3]. In general, the structure of a DSSC consists of a dye-adsorbed nanocrystalline TiO₂ photoanode, an electrolyte, and a counter electrode [4,5].

The counter electrode serves an important and indispensable role in collecting electrons from an external circuit and reducing I₃⁻ to I⁻ for the regeneration of sensitiser after electron injection [6].

Typically, platinum (Pt) and Pt-based metallic structures are used as counter electrodes due to their high electrochemical activity. However, Pt is a noble metal and relatively expensive. Moreover, the slow dissolution of the Pt counter electrode in the corrosive I₃⁻/I⁻ redox electrolyte deteriorates the long-term DSSC stability [7]. Therefore, replacement of Pt with other cheaper material was required for the reduction of production cost of the cells.

Recently, carbon materials, in the forms of activated carbon [8], carbon black (CB) [9], graphite [10], carbon nanotubes (CNTs) [11,12] and graphene (GN) [13,14], have become potential materials to substitute for Pt, because of their low cost, high conductivity, and good catalytic ability for the reduction of I₃⁻ ions. Among them, GN [15] has been utilised as the catalytic film on the counter electrode of DSSCs [16,17]. For example, Roy-Mayhew et al. [18] fabricated a DSSC with functionalised GN on its counter electrode and reached an efficiency of 5.0%, which was comparable to that of a cell with a typical Pt counter electrode (5.5%). In addition, GN has several unique physicochemical properties, such as strong mechanical strength, good conductivity and high electron mobility ($\sim 200,000 \text{ cm}^2/\text{V s}$) [19,20], and it has drawn significant attention for its engineering applications [21,22]. Dispersing GN in base fluid is very difficult due to the high specific surface area and $\pi-\pi$ interactions; therefore, improving the dispersion of GN in the matrix is essential to its successful application in DSSCs.

In this article, acid oxidation and planetary ball milling were used to improve the dispersibility of GN in an ethanol solution. Based on the previous work of Munkhbayar et al. [23], wet grinding with a rotation speed of 500 rpm was used in the present study. Furthermore, we investigated the performances of DSSCs with three different GN structures (raw, purified, and purified and ground at 500 rpm) that were spin coated onto FTO-coated glass substrates for use as counter electrodes. The photovoltaic efficiency of DSSCs with GN counter electrodes was successfully improved by the acid oxidation and planetary ball milling approaches compared to that of DSSCs with a raw GN structure. The improved photovoltaic efficiency of the DSSCs with GN counter electrodes was still lower than that of a DSSC with a costly Pt counter electrode. Therefore, additional work was needed to find other materials that are readily available and cost effective and that could demonstrate comparable catalytic effects for the triiodide reduction in DSSCs.

Recently, tungsten carbides (WC) have been used as electrocatalysts because of their platinum-like catalytic behaviour, high stability, and low electrical resistance [24,25]. In particular, carbides of group IV–VI metals show catalytic performances similar to those of platinum-group metals in a variety of reactions involving hydrogen [26]. Unfortunately, the photovoltaic efficiency of DSSCs prepared with only WC particles was not comparable to that of DSSCs with Pt electrodes [27,28]. Therefore, several reports are available with GN [13] or tungsten [29,30] used solely as a counter electrode for DSSCs, but a GN–tungsten composite structure as an alternative to Pt counter electrodes has not been previously investigated.

In this paper, a GN–tungsten composite structure, with a highly improved dispersibility of GN in an ethanol solution, was synthesised and used as a counter electrode for DSSCs. The counter electrodes were spin coated onto FTO glass and the

thickness and surface roughness of the particles were controlled by simply adjusting the parameters (i.e., rotation speed, time, catalyst, etc.) [31]. DSSCs fabricated with the GN–tungsten composite structure showed a high photovoltaic efficiency of 5.88%, which was similar to that of a cell with a conventional Pt electrode (5.92%). The significance of a cell with the composite film of GN–tungsten implies in the fact that an expensive Pt is avoided; thereby the cost of pertinent DSSC is greatly reduced.

2. Experimental details

2.1. Materials

GN and tungsten structures were used as the main materials in this study. GN (AO-2) with a specific surface area (SSA) of 100 m g⁻² and 99.9% purity (purchased from Graphene Supermarket, USA) was used as the GN source. The GN has an average thickness of 8 nm (consisting of 20–30 monolayers) and a lateral size of averaging 550 nm. The tungsten nanoparticle with a mean size of 100 nm and 99.9% purity was obtained from Nanotechnology Inc., Korea. A platinum precursor (10 mM), Ru complex dye (N719), cis-bis (isothiocyanato) bis (2, 2'-bipyridyl-4, 4'-dicarboxylato)-ruthenium (II) bis-tetrabutylammonium, ethyl cellulose, terpinol and iodolyte AN-50 (iodide-based redox electrolyte) were purchased from Solaronix Co., Ltd., Switzerland.

2.2. Preparation of the raw, purified, and purified and ground structures of graphene, tungsten and graphene–tungsten composite

Generally, the raw GNs have a hydrophobic surface [32], which is prone to aggregation and precipitation in base fluids in the absence of a dispersant/surfactant. For better dispersion, raw GNs were purified by simple method that using nitric acid (HNO₃) and sulphuric acid (H₂SO₄) with concentration of 63% and 98% (1:3 v/v), respectively was employed. The detailed purification process of acid oxidation was previously described [23], which was applied on carbon nanotubes. Purification was performed by ultrasonication 1510E-DTH (Branson Ultrasonic Corporation 41, USA) for 5 h to remove the impurities and to improve exterior activity. Calorimetry was performed to measure the output power and frequency of the applied ultrasonic vibration (63 W and 42 kHz, respectively). The production sample is named as the purified GN, which was used for next step in the experiment.

In our previous study [33], we found that only the purified structure showed incomplete dispersion stability of CNTs in base fluid. Based on the previous work [33], the purified GN structure was ground under wet condition at a rotation speed of 500 rpm for 1 h. In the present study, a planetary ball mill (HPM-700) (Haji Engineering, Korea) was used to grind the sample. Monosized (3.0 mm) spherical zirconia (ZrO₂) balls were used as the collision medium. Grinding process was performed as following published literature [33]. The direction of the pot rotation was set counter to that of the disk revolution. The configuration of the planetary ball mill is shown in Fig. 1. The resulting structure is termed as purified and ground GN.

In this experiment, tungsten nanoparticles were used as received. The purified and ground GN and tungsten structures were mixed at room temperature. It is well known that ultrasonication is generally used to disperse particles in base fluid. To enhance the dispersion, the previously prepared five structures, namely raw, purified, purified and ground GN, tungsten, and GN–tungsten composite, were ultrasonicated in anhydrous ethanol for 40 min. The concentrations of the particles (50% GN: 50% tungsten) in ethanol were 2.0 wt%.

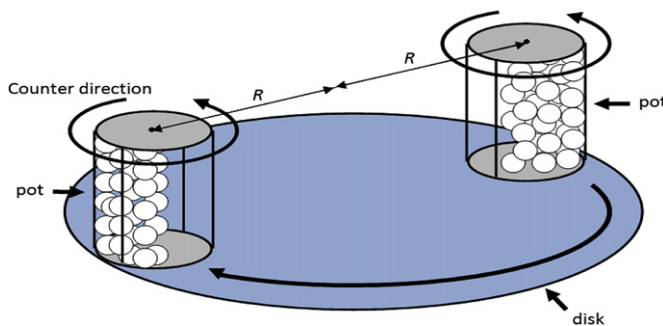


Fig. 1. The configuration of a planetary ball mill.

2.3. Fabrication of the counter electrodes

To remove organic pollutants and other contaminants, the FTO glasses ($20\text{ mm} \times 20\text{ mm} \times 2.2\text{ mm}$ dimensions), with a sheet resistance of $8\text{ }\Omega\text{ sq}^{-1}$, were ultrasonicated and thoroughly cleaned in acetone, ethanol and distilled water, for 15 min in each step. The previously prepared five different fluids, containing raw, purified, and purified and ground structure of GNs, tungsten, and GN–W composite, were deposited on the cleaned FTO glass using the spin coating (Spin coater JSPA type) method. For a comparison with the above five counter electrodes, 10 mM platinum precursor was deposited on cleaned FTO glass by spin coating at 2000 rpm for 30 s at room temperature. Ethanol-based solutions containing 2 wt% of above structures used for depositing the corresponding films on FTO glasses, by drop coating technique. Then, the fabricated counter electrodes were heated at $350\text{ }^\circ\text{C}$ for 15 min to maintain good adhesion between the particle layer and FTO substrate. Notably, if the annealing temperature of the deposited carbon based (CNTs, GNs) films were higher than $400\text{ }^\circ\text{C}$, the terpineol and ethyl cellulose might be completely evaporated; however, the GNs films would be easily peeled from the substrate [34]. Thus, a tradeoff between increasing the adhesion and increasing the electrical conductivity exists. Considering this tradeoff, an annealing temperature of $350\text{ }^\circ\text{C}$ was used to prepare the GNs-based counter electrodes. The performances of GNs-coated samples were compared to a conventional Pt coated electrode. An experimental condition of counter electrodes is displayed in Table 1.

2.4. Preparation of TiO_2 nanocrystalline films and fabrication of the DSSCs

Firstly, the TiO_2 paste was prepared as mentioned [34]. The TiO_2 electrode was used in the conventional method in this experiment to fabricate the working electrode. The TiO_2 working electrodes were fabricated using the prepared TiO_2 paste on FTO glass using a screen-printing technique. The TiO_2 paste was fabricated and deposited on FTO glass with an approximate $10\text{--}12\text{ }\mu\text{m}$ thickness and $1.0 \times 1.0\text{ cm}^2$ surface area. The fabricated TiO_2 electrode was

then subjected to $150\text{ }^\circ\text{C}$ for 30 min and subsequently calcined at $500\text{ }^\circ\text{C}$ for 1 h in air to obtain an anatase TiO_2 phase. Then, the TiO_2 working electrodes were immersed in a 0.3-mM solution of a Ru complex dye (N719) for 24 h to ensure that the dye molecules were fully absorbed. The DSSCs were comprised of a sensitised working electrode, various counter electrodes and an electrolyte, with a $60\text{ }\mu\text{m}$ thick hot-melt sealing foil between each layer. The electrolyte, iodolyte AN-50, was introduced into the cell by vacuum, filling through an injection hole on the counter electrode side. Finally, the electrolyte injection hole was sealed with Surlyn and a microscope glass cover.

2.5. Characterisation and measurements

The current study is compared dispersibility and light absorption of the five different structures that were dispersed in ethanol, and their stabilities were determined with an ultraviolet-visible (UV-vis) spectrometer (X-ma 3000 Series) at wavelength ranging between 400 and 800 nm. Transmission electron microscopy (TEM) (JEM-2100F, JEOL) was used to observe the structural characterisation of samples. The surface morphologies and thicknesses of counter electrodes were investigated by a scanning electron microscopy (SEM) (JSM-6710F, JEOL). Before observing the cross section of counter electrodes, a cross section polisher (IB-09020CP, JEOL) was used to polish the electrodes. X-ray diffraction (XRD) measurements were taken with a Bruker AXS, D8 advance powder diffractometer, using $\text{Cu K}\alpha$ radiation ($\lambda = 1.5406\text{ \AA}$). The samples were rotated at 10 rpm and swept from $2\theta = 10^\circ$ through to 90° using default parameters of program of the diffractometer that was equipped with Bruker AXS Diffrac PLUS software. In addition, structural changes of the processed samples were examined by Labram HR800 Raman spectrometer with a 514 nm Argon ion laser. Raman spectra were recorded in the Raman shift ranging from 1200 to 1700 cm^{-1} . Fourier transform infrared (FT-IR) measurement (Vertex 80 V, Bruker) was used to realise the chemistry structure of raw and purified GNs. For the FT-IR spectral record, a spectrometer (Bruker) was used to record its spectral data in the $400\text{--}4000\text{ cm}^{-1}$ frequency ranges by accumulating 128 scans with a resolution of 2 cm^{-1} . Accelerated Surface Area and Porosimetry System (ASAP 2020) was used to measure Brunauer, Emmett, and Teller (BET) surface area of GNs particles. The photocurrent–voltage ($J\text{--}V$) characteristics of the DSSCs were measured under simulated solar illumination with a light intensity of 100 mW cm^{-2} (AM 1.5G) using a solar module analyzer Prova-200.

3. Results and discussion

3.1. Characterisation of the raw, purified, and purified and ground structures of graphene

The surface morphologies of the GN materials were investigated by TEM. Fig. 2 shows TEM images of the (A) raw, (B) purified and (C)

Table 1
Experimental condition of counter electrodes of DSSCs.

Label	Structure of CEs	Conc. (50% GN: 50% W)	Treatments and condition	Annealing temperature	Coating method and condition
Electrode 1	Raw GNs	2.0 wt%	Ultrasound	$350\text{ }^\circ\text{C}$	Spin coating (R. speed: 2000 rpm
Electrode 2	Purified GNs	2.0 wt%	$\text{H}_2\text{SO}_4 + \text{HNO}_3$ & ultrasound	$350\text{ }^\circ\text{C}$	R. time: 30 s)
Electrode 3	Purified & ground GNs	2.0 wt%	$\text{H}_2\text{SO}_4 + \text{HNO}_3$ & grinding (500 rpm) & ultrasound	$350\text{ }^\circ\text{C}$	
Electrode 4	Tungsten	2.0 wt%	Ultrasound	$350\text{ }^\circ\text{C}$	
Electrode 5	GNs & tungsten composite	2.0 wt%	Electrode 3 + electrode 4 & ultrasound	$350\text{ }^\circ\text{C}$	
Electrode 6	Standard Pt	10 mM	As-received	$350\text{ }^\circ\text{C}$	

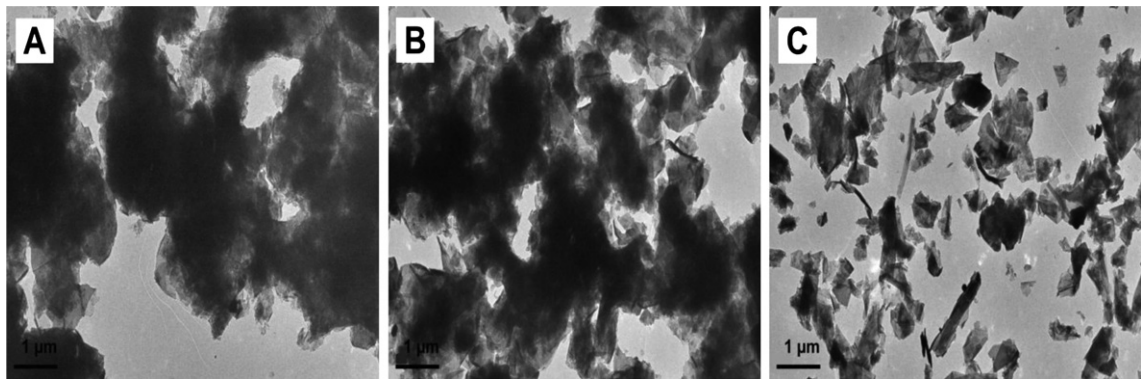


Fig. 2. TEM images of (A) raw, (B) purified and (C) purified and ground GN films.

purified and ground GNs in ethanol solution. As shown in Fig. 2A, the raw GN appears densely agglomerated and in a larger planar structure. The agglomeration of the GN could have been due to the lack of hydrophilic groups and the strong $\pi-\pi$ stacking interactions on its surface [32]. In contrast, Fig. 2B shows that the agglomeration rate of GN was slightly decreased after acid oxidation. The decreased agglomeration of the purified GN was because of the presence of hydrophilic groups (e.g., hydroxyl, epoxy, or carboxyl) on its surface. Indeed, no aggregated particles and an improved SSA of GN were observed after employing the grinding method, as shown in Fig. 2C. The large GN aggregated particles were separated into several individual GNs; therefore, the SSA was highly improved. This improved structure of purified and ground GNs was due to the high-energy ball milling.

It should be noted that aggregation would reduce the electrochemical catalytic activity towards the reduction of tri-iodide ions, decreasing the photovoltaic efficiency. To further improve the performance of DSSCs, particles should be dispersed without agglomeration in base fluid [34]. Fig. 3 shows the photographs of raw, purified and purified and ground GN structures that were dispersed in ethanol, and the stabilities of the dispersions were observed 12 h after ultrasonication. As shown in Fig. 3A, because of the aforementioned lack of hydrophilic groups in their structure prohibiting interaction with the polar solvent, the dispersion state of raw GN shows large amounts of aggregated particles that were attached on the wall of the bottle instead of being dispersed, despite the application of ultrasonication. In contrast, Fig. 3B shows

the dispersion state of the purified GN structure in an ethanol solution following ultrasonication, which shows the nearly complete dispersion of purified GNs in base fluid. It also shows that the purified GN in ethanol was unstable, consisting of a negligible amount of both aggregation and precipitation. Therefore, the presence of hydrophilic groups on the surface of the particles could improve dispersion; the aggregations are generally insufficient to allow complete dispersion because of a large hydrophobic surface area [33]. The purified and ground GNs exhibited an optimal stable dispersion with no precipitation and no agglomeration occurring at room temperature, as shown in Fig. 3C. This optimal stable dispersion was due to the removed agglomeration using a wet grinding approach. To further study the mechanism of the dispersibility improvement, the different GNs structures were examined by XRD analysis.

After the treatment processes, it is essential to keep the crystallographic structures of the materials for its next application.

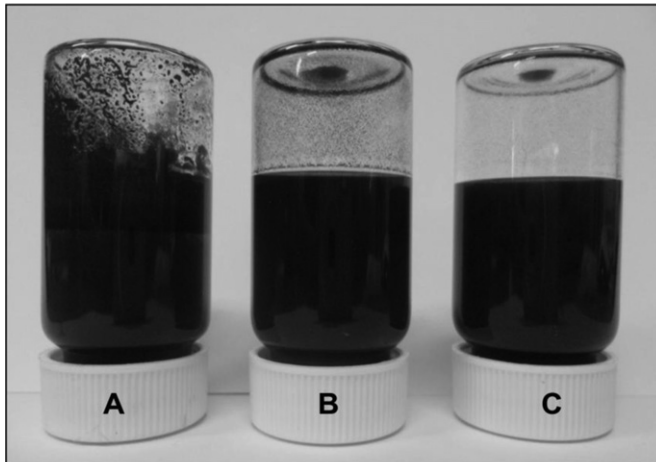


Fig. 3. Photographic images of (A) raw, (B) purified and (C) purified and ground GNs in ethanol.

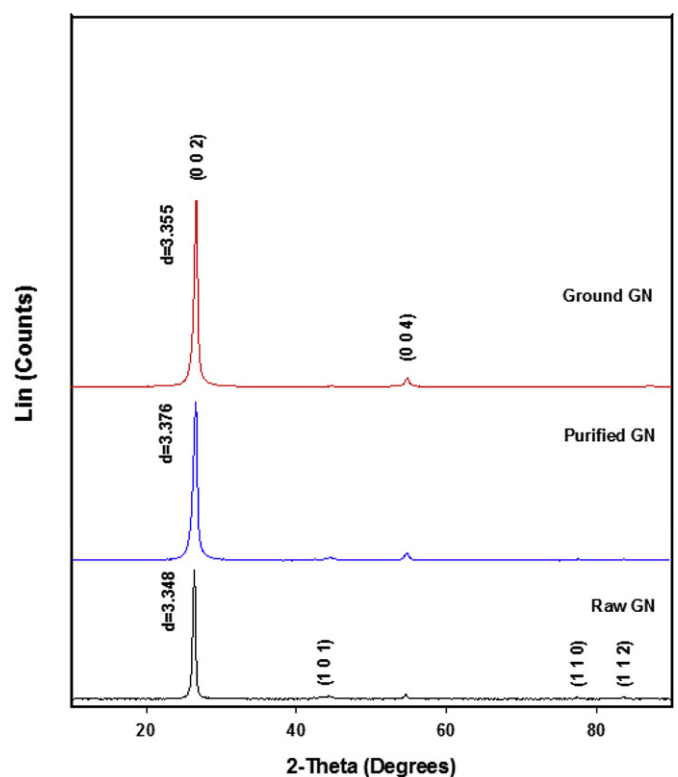


Fig. 4. XRD patterns of three different GN structures.

Fig. 4 shows XRD patterns of the raw, purified and purified and ground GN samples. As shown in Fig. 4, the pronounced (0 0 2) peaks at about 26.5° and (0 0 4) peaks at about 54.6° were observed for the all GN samples and were assigned to the layer-to-layer distance (d -spacing: $d = \lambda/2 \sin \theta$). The interlayer spacing of raw GN ($d = 3.348 \text{ \AA}$) was increased after acid oxidation of the GN ($d = 3.376 \text{ \AA}$). This increment occurred because of the presence of hydrophilic groups (e.g., hydroxyl, epoxy, or carboxyl) on its surface, which can improve the dispersibility of GNs in base fluid [32]. In contrast, when compared to the purified GN, the interlayer spacing of purified and ground GN was slightly decreased to $d = 3.355 \text{ \AA}$, which was attributed to the impact of high-energy ball milling. In addition, the XRD pattern of the raw GN sample depicted a weak intensity (1 0 1) peak at $2\theta = 44.4^\circ$, (1 1 0) peak at $2\theta = 77.2^\circ$ and (1 1 2) peak at $2\theta = 83.2^\circ$. These weak peaks were due to some impurities, such as soot, metal and/or amorphous carbon [35]. Fig. 4 shows that the weak peaks were not observed in the XRD patterns of purified, and purified and ground GNs samples. This indicates that the impurities were completely removed after the acid oxidation and grinding processes. Moreover, the XRD results ensured that the crystallographic structure of the GNs remained unchanged after the acid oxidation and grinding processes.

Raman spectroscopy is a useful tool for investigating the structural variations that occur in carbonaceous materials because it shows both the D band and the G band [36]. Fig. 5 shows the position of various peaks of the band and the D/G ratios for the three different GN structures. As shown in Fig. 5, the Raman spectrum of three GNs samples had the characteristic G-band at a Raman shift of 1580 cm^{-1} and a very weak D-band at 1353 cm^{-1} . The former was due to the vibration of sp^2 -bonded carbon atoms in a 2D hexagonal lattice [37,38] and the latter was caused by the vibrations of carbon atoms with dangling bonds of in-plane terminations of disordered graphite [37]. It is worth noting that

no changes in the polycrystalline characteristics of the GNs occurred. Moreover, the D/G ratio changes were generally caused by (a) an increase or decrease in the amount of amorphous carbon, (b) a higher defect density, or (c) a decrease in the crystalline size [39]. Fig. 5 shows that the D/G ratio of raw GN (0.32) increased after the acid oxidation of GN (0.47). This increment in the D/G ratio was due to the oxidation and sonication processes resulting in the formation of GN with several oxygenated functional groups, such as carbonyl, carboxyl, hydroxyl, and epoxy groups. Compared to only the purified GN, the D/G ratio of purified and ground GN (0.57) was slightly increased due to the effect of high-energy ball milling [40]. Finally, the XRD and Raman results are in good agreement with Lee et al. [40].

Fig. 6 shows FTIR spectra of raw and purified GNs. The FT-IR spectrum of raw GN is almost featureless with weak skeletal vibrations of aromatic domains around $1590\text{--}1610 \text{ cm}^{-1}$, which is in agreement with observations [41,42]. FT-IR spectra of purified GN material, as featured for graphene oxide by a strong absorption band at 1677 cm^{-1} due to the $\text{C}=\text{O}$ stretching, a broad band at 3410 cm^{-1} (ν_{OH}), a very strong peak at 1587 cm^{-1} ($\nu_{\text{C}=\text{C}}$), a weaker peak at 1420 cm^{-1} (δ_{OH}), and a band at 1090 cm^{-1} ($\nu_{\text{C}-\text{O}-\text{C}}$) [42].

UV-absorption spectra were used to determine the dispersion characteristics of the suspensions [23]. It is well established that higher absorbance values generally indicate an enhanced dispersibility of particles in solution [32–34]. To optimise the dispersion characteristics of the materials, a standard Pt solution and the previously prepared three different GNs samples were studied using a UV-spectrometer. Fig. 7 depicts the UV-absorption spectra at wavelengths ranging from 400 nm to 800 nm of the standard Pt solution (10 mM Pt in ethanol) and the raw, purified, and purified and ground GN structures that were dispersed in an anhydrous ethanol solution (0.05 wt% GN in ethanol). The UV light absorbance of the standard Pt solution was measured to be lower than those of the GNs solutions because metallic Pt particles reflect most of the light. In general, the GNs are opaque, black, and light-absorbing materials, which absorb more of the higher UV light between the wavelengths ranging between 400 nm and 800 nm

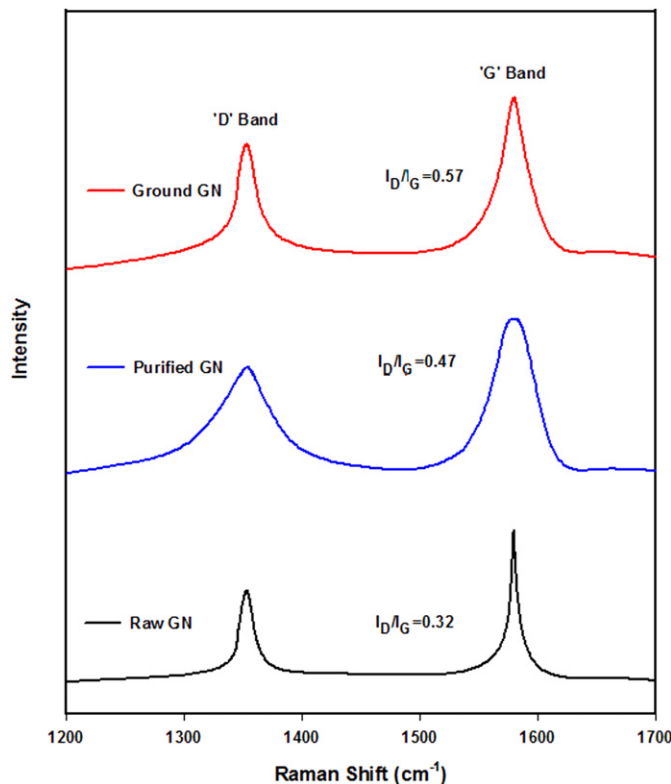


Fig. 5. Raman spectra of three different GN structures.

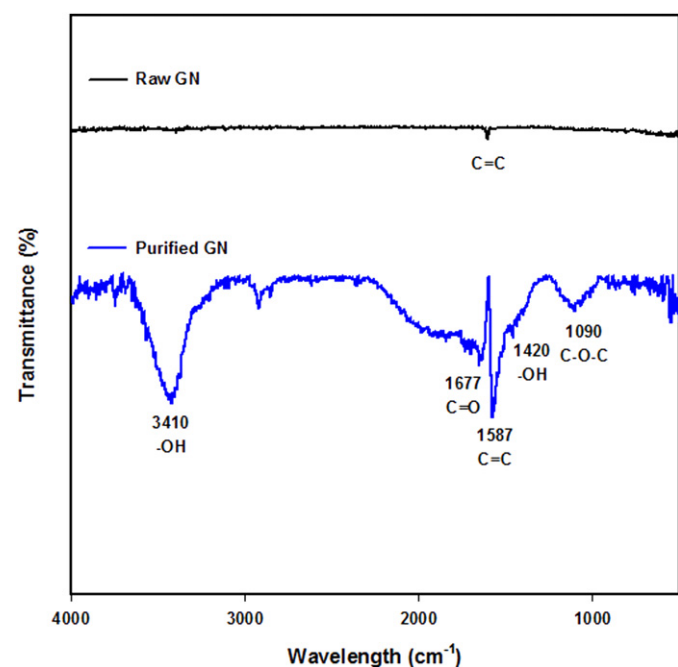


Fig. 6. FT-IR spectra of raw and purified GN structures.

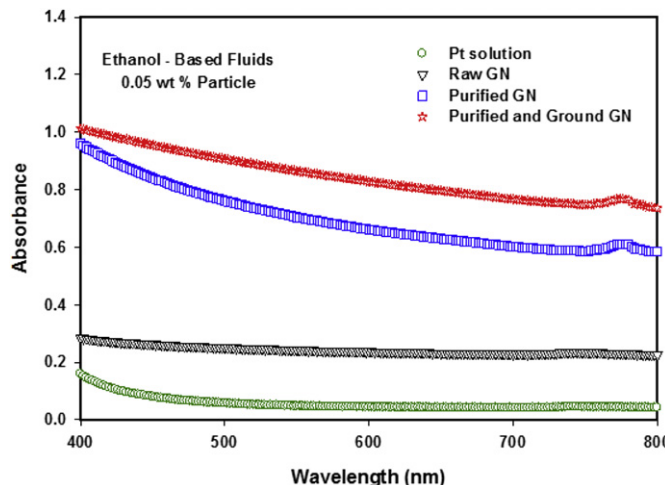


Fig. 7. UV-vis spectra of a standard Pt solution and raw, purified, and purified and ground GN structures in ethanol (0.05 wt%).

than that of the Pt solution. The absorption of photoelectron value would be enhanced with increased light absorption. Contrastingly, the UV light absorbance values of purified GN in ethanol solutions were higher than those of raw GNs in ethanol, despite the same experimental conditions. Thus, the purification of GN removed the impurities and agglomerations of raw materials; consequently, the purified structure allowed GNs to disperse well in base fluid. The UV light absorbance values of the purified GNs in ethanol solutions did not indicate optimal dispersion. When comparing the four different suspensions, the purified and ground GNs in ethanol obtained the highest UV light absorption because of their improved dispersibility. Grinding produced optimal dispersions of GNs in base. The improved dispersibility of GN in base fluid by using the ball milling method can be explained by the fact that grinding can break up large GN aggregates into smaller aggregates, and further, exfoliation can be employed to break these smaller aggregates into individual particles, which can facilitate the use of ultrasonication to disperse GNs [43]. Individual GN particles would be well dispersed in base fluid, which is significant for practical application. The detailed discussion for the improvement of dispersibility was clearly described in our previous article [23]. These findings show that the purification and grinding processes can significantly improve the dispersion of GNs in ethanol.

3.2. DSSC photovoltaic characteristics of the GN counter electrode structures

The working principle of DSSCs is reported in literature [33,34]. At the counter electrode, an energy-efficient DSSC tri-iodide should be efficiently reduced to iodide. The counter electrode must be catalytically active to ensure a rapid reaction. The counter electrode must also be a strong conductor and exhibit a low over potential for the rapid reduction of the redox couple to transport the photocurrent across the width of each solar cell. Hence, aside from the specific surface areas and the adhesion between the counter electrode layer and the FTO substrate, the work function and electron binding energy of GN exert their influence on the photovoltaic performance [44]. The work function is one of the basic physical quantities required to determine the electronic structure and interaction of the GN/metal interface [44].

The photovoltaic performance of DSSCs can be improved by increasing the SSA and electrochemical activity of the counter electrode, which can increase the I_3^-/I^- redox reaction rate [45]. The

electrochemical activity of GNs can be explained in terms of the SSA; the large surface area of carbon materials can enhance electrochemical activity. Moreover, the angstrom-wide tri-iodide ions have a greater probability to diffuse into the pores, be absorbed onto the active site and become reduced. This result suggests that carbon based counter electrodes have a highly electrochemical active surface [46]. Hence, aside from improving the dispersibility of GNs in base fluid, increasing the SSA is essential to further improve the performance of DSSCs.

Fig. 8 shows the BET surface area of raw, purified and purified and ground GNs. The BET specific surface areas were 112.2, 124.11 and 203.95 $m^2 g^{-1}$ for the raw, purified and purified and ground GNs, respectively. As shown in Fig. 8, the BET surface area of GN was slightly improved after acid oxidation. The improved BET surface area of purified GN was caused by the decreased agglomeration of the raw material. Specifically, the surface area of the purified and ground GN was approximately 81.5% greater than that of the non-ground GN. The increase in the BET specific surface area indicates that grinding method had an effect on the surface area or the generated porosity [40]. It should be noted that the grinding method was an effective method for increasing surface area, thereby significantly reduced the agglomeration of particles [33]. The possible reason for the BET surface area improvement of the carbon and GN materials by employing the ball milling method has been previously reported [40,43,47,48]. For example, Lee et al. [40] studied the SSA of CNTs improved by a milling machine. The authors reported that with increasing SSA and pore volume, the pore diameter of the milled CNTs decreased with increasing milling speed when compared to that of un-milled CNTs. The larger SSA was due to the more open tips and increased pore volumes than those for smaller surface areas. Moreover, during the grinding process, the powder mixture was subjected to high-energy, inter-particle and milling-ball collisions at high rotation speeds. Consequently, individual MWCNT particles were formed and SSA improvements with increasing grinding speed were observed in our previously published work [43].

The characteristics of the counter electrode should have an effect on the efficiency of the solar cell, and the counter electrode control revealed a high performance photocurrent–voltage measurement because of its low resistance. To promote a highly conductive counter electrode, a dense and uniformly coated GN layer is essential. Fig. 9 illustrates the cross sectional SEM of the counter electrodes with different GN structures, which shows relatively different adhesion between GNs and FTO glass substrates. As shown in the cross sectional SEM of the counter electrode in

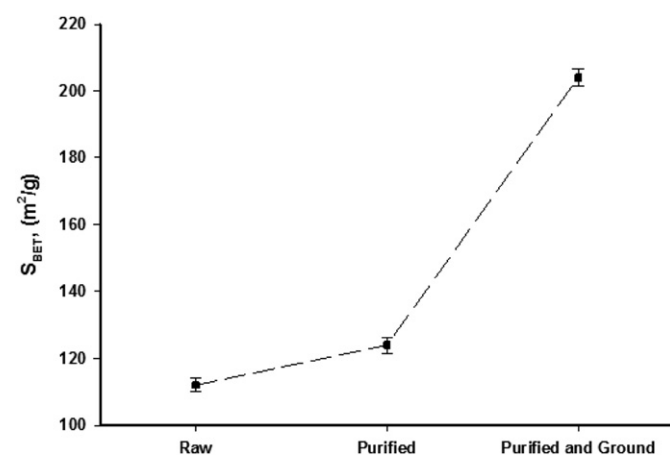


Fig. 8. The BET specific surface area of raw, purified and purified and ground GNs.

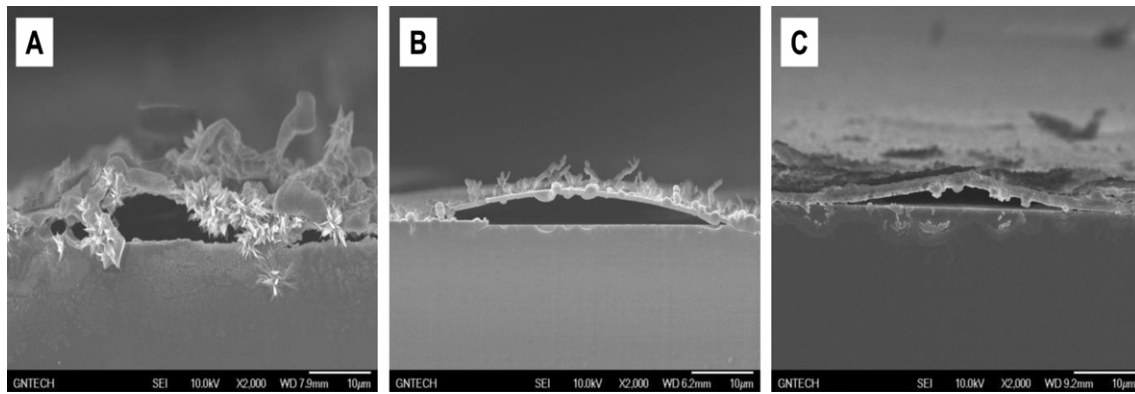


Fig. 9. Cross sectional SEM images of the (A) raw, (B) purified and (C) purified and ground GNs.

Fig. 9A, the raw GN was densely agglomerated with a very rough surface and exhibited non-uniform layers. The adhesion of GN to the glass substrate was very poor due to the poor dispersibility of the raw GN in ethanol solution, as described above. In contrast, it can be observed from Fig. 9B that the agglomeration of the purified GN structure on the FTO glass substrate was decreased due to its improved dispersibility by acid oxidation. A deposited layer was not required to be uniform due to an incomplete dispersion of purified GN in the ethanol solution. A very large gap and slot were observed between the purified GN layer and its substrate, as shown in Fig. 9B. When compared to the raw GN counter electrode, a slight improvement was observed. In Fig. 9C, no aggregated particles were observed because of the improved dispersibility of the GN suspension, as described above. The adhesion of purified and ground GN particles to a glass substrate was highly improved when compared to those of the raw and purified GN counter electrodes. Therefore, the gap and slot size of the purified and ground GN layer and its substrate were decreased due to the improved SSA of the GN after grinding. The purified and ground GN particles were incompletely adhered to the glass substrate; a very small gap and slot were still observed between the GN layer and its substrate, which may be attributed to the structure and planar shape of the GN particles [34].

From the above discussions, it is expected that the photovoltaic performances of the DSSCs with the purified and ground GN structure counter electrode will show higher values than those of the DSSCs prepared with the raw and purified GN structure counter electrodes. The photocurrent–voltage (J – V) characteristics of the DSSCs with raw, purified and purified and ground GN, and standard Pt counter electrodes are shown in Fig. 10, and the corresponding photovoltaic parameters are summarised in Table 2. As shown in Fig. 10 and Table 2, the open-circuit photovoltage (V_{oc}), short-circuit photocurrent (J_{sc}), fill factor (FF), and the energy conversion efficiency (η) of the DSSCs with GN were greatly increased corresponding to their dispersion characteristics. The energy conversion efficiency (η) of DSSCs with raw, purified and purified and ground GNs counter electrodes were 2.71%, 3.18% and 4.55%, respectively. Each value was significantly improved after applying the purification and grinding methods. The reasons for the photovoltaic performance improvements of DSSCs with purified and ground GN counter electrode are due to the following aspects: (i) the increased SSA (Fig. 8) of the GN counter electrode may promote the reaction of I_3^- reduction at the interface between the GN and electrolyte, thus improving the J_{sc} [45,49,50]. (ii) It is well known that increasing the SSA of GN can also enhance the electrochemical activity [33,49]. Moreover, higher GN electrochemical activity produces higher V_{oc} values. (iii) Of the concerned GN structures,

the adhesion of the purified and ground GN layer to a glass substrate was most likely greater than those of the raw and purified GN counter electrodes (Fig. 9). This enhanced adhesion of GN to the substrate provided fast electron-transport channels for I_3^- reduction. Furthermore, GN provided a rapid diffusion pathway for the redox electrolyte and improved the contact between the counter electrode and electrolyte, enhancing the electron transfer rate at the counter electrode and electrolyte interface, which increased the FF [50]. In addition, one of the possible reasons for the improved η of the DSSCs with a purified and ground GN counter electrode was that the increased dispersibility of the purified and ground GN structure in ethanol exhibited more high light absorption (Fig. 7), which harvested fast redox kinetics because of a greater photo-induced electron density. The η of DSSCs with a GN counter electrode were still lower than that of DSSCs with a standard Pt counter electrode, despite the η improvement from the acid oxidation and grinding processes. Compared to the Pt-based DSSC, the lower photovoltaic efficiency of DSSCs with GN counter electrodes may be attributed to the particle loading. The particle loading also influenced the textural properties (including SSA, porosity and pore volume) and the optical absorption properties [51,52]. For example, Fan et al. [52] investigated the effects of graphene on the microstructures and photovoltaic performance of DSSCs. It was noted that a moderate amount of graphene (<0.75 wt%) obviously enhanced DSSC efficiency, but they found that higher graphene

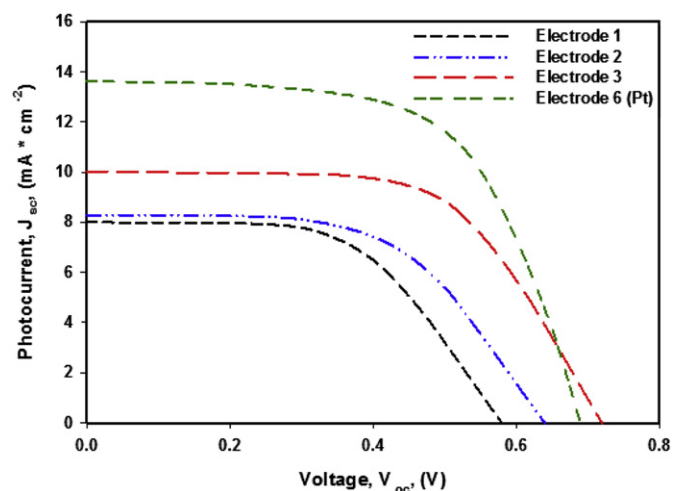


Fig. 10. The photocurrent–voltage (J – V) characteristics of the DSSCs fabricated using a Pt film and various GN counter electrodes.

Table 2

The $J-V$ curve characteristics of DSSCs with various GNs counter electrodes.

Counter Electrode	J_{sc} (mA cm^{-2})	V_{oc} (V)	FF	η (%)
Electrode 1	8.00	0.58	0.58	2.71
Electrode 2	8.28	0.64	0.59	3.18
Electrode 3	10.02	0.72	0.63	4.55
Electrode 6 (Pt)	13.62	0.69	0.63	5.92

loading not only impaired the crystallinity of the TiO_2 -NSs but also shielded the light adsorption of the dyes and reduced the number of photogenerated electrons. To further improve the performance of DSSCs with GN structures, we introduced tungsten nanoparticles as an additive material. Among the three different GN counter electrodes, considering the photovoltaic performance of the DSSCs, the purified and ground GN structure was selected and used for the further experiments.

3.3. Characterisation of the graphene, tungsten and graphene–tungsten composite structures

In the present work, the GN structure was incorporated with tungsten nanoparticles in an ethanol solution using ultrasonication. Fig. 11 shows high resolution TEM images of GN, tungsten and GN–tungsten composite. Basically, GNs with an area of several micrometres resembled a transparent silk, as shown in Fig. 11A, and this morphology of GN remained unchanged after the acid oxidation and grinding processes. Fig. 11B shows tungsten nanoparticles having spherical shapes with diameters smaller than 100 nm. A typical TEM image (Fig. 11C) of the tungsten–GN shows the binding of tungsten to GN. Fig. 11C shows a homogeneous dispersion of tungsten in the GN matrix that was eager to accumulate along the wrinkles and edges of the visible graphene sheets. The tungsten nanoparticles were not simply blended with GNs; rather, they were possibly entrapped inside the GN sheets. Therefore, these tungsten particles were likely to interact with the GN via carboxylic acid functional groups or simple physisorption. Moreover, the preparation of the GN-based composite was reported [53–55].

To further confirm the composition of the GN, tungsten and GN–tungsten composite, XRD analysis was conducted. Fig. 12 shows two broad diffraction ($0\ 0\ 2$) and ($0\ 0\ 4$) peaks at approximately $2\theta = 26.5^\circ$ and $2\theta = 54.6^\circ$, respectively, corresponding to the GN structure. Therefore, the five broad diffraction ($1\ 1\ 0$), ($2\ 0\ 0$), ($2\ 1\ 1$) and ($2\ 2\ 0$) peaks at approximately $2\theta = 40.3^\circ$, $2\theta = 58.3^\circ$, $2\theta = 73.2^\circ$ and $2\theta = 87.0^\circ$, respectively, were observed for the tungsten structure. Moreover, several small diffraction peaks were also assigned to the β -tungsten. The XRD pattern of the GN–tungsten composite exhibited all the characteristics of diffraction

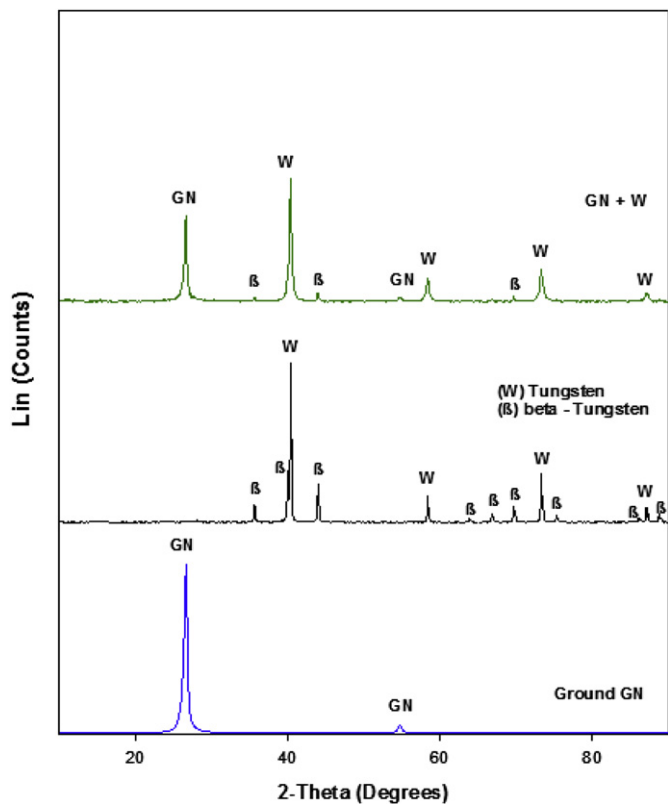


Fig. 12. XRD patterns of the GN, tungsten and GN–tungsten composite structures.

peaks of GN and tungsten structures at $2\theta = 26.5^\circ$, $2\theta = 40.3^\circ$, $2\theta = 54.6^\circ$, $2\theta = 58.3^\circ$, $2\theta = 73.2^\circ$ and $2\theta = 87.0^\circ$. TEM and XRD results demonstrated that the GN–tungsten composite was successfully synthesised.

It should be noted that the light absorption spectra for DSSCs generally display a similar topography in the wavelength range of 400–800 nm. Fig. 13 depicts the UV light absorption spectra at wavelengths ranging 400 nm–800 nm of the GN, tungsten and GN–tungsten composite structures that were dispersed in ethanol (0.05 wt%). As shown in Fig. 13, UV light absorbance of the GN in ethanol was measured to be lower than those of the tungsten and GN–tungsten composite solutions. It is well known that the UV–vis spectra of carbon based materials and GN structures in base fluid are strongly active at wavelengths at approximately 265 nm [43,56]. Conversely, GN is hardly active in the wavelength region from 400 to 800 nm [56]. Fig. 13 shows that the highest UV light

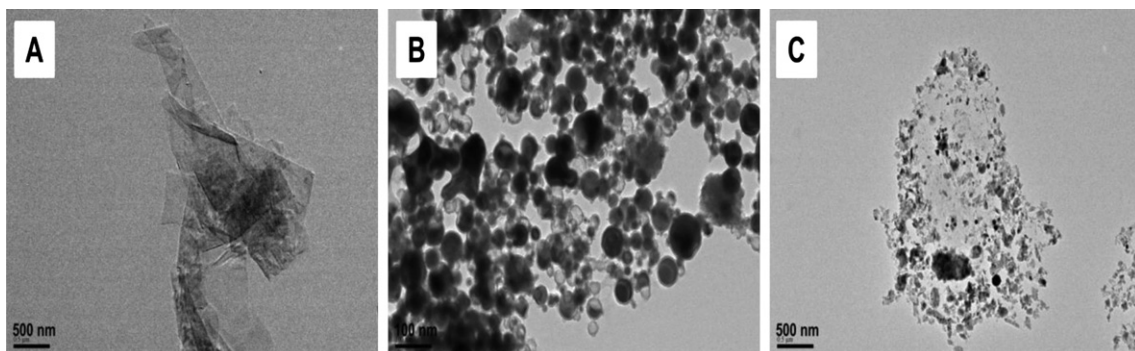


Fig. 11. HRTEM images of the (A) GN, (B) tungsten and (C) GN–tungsten composite.

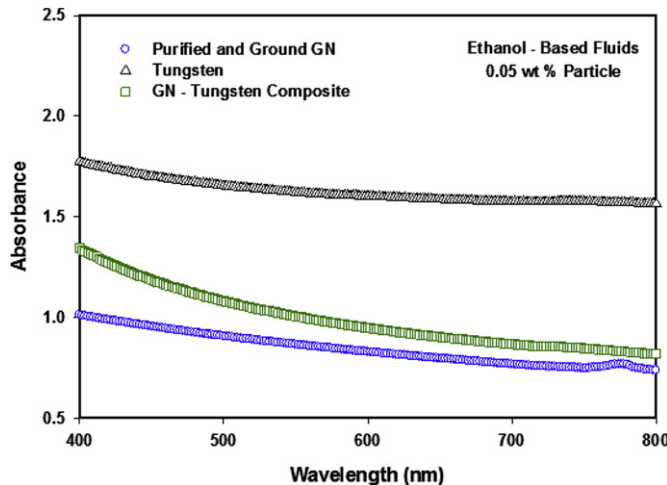


Fig. 13. UV-vis spectra of CN, tungsten and GN–W composite structures in ethanol (0.05 wt%).

absorbance was recorded for the tungsten structure in ethanol. Generally, the tungsten-based sample showed a high UV–vis absorbance at wavelengths ranging between 400 and 800 nm [57]. This high light absorbance may support the increased photovoltaic performance. Indeed, because of the high light absorbance of tungsten, the UV light absorbance of the GN–tungsten composite structure in ethanol was slightly higher than that of the GN sample, which is an advantage for CNTs in DSSC applications. It should be noted that the enhancement of visible light absorption means an increase in the light-harvesting capability of the electrodes [58].

Fig. 14 illustrates the cross sectional SEM of the GN, tungsten and GN–tungsten composite counter electrode structures, which shows a relatively different adhesion of particles to glass substrates. It was previously mentioned that the treated GN particles incompletely adhered to a glass substrate; a small gap and slot were observed between the GN layer and its substrate, as shown in Fig. 14A. In contrast, Fig. 14B shows that the adhesion of tungsten nanoparticles to the substrate was not required to be complete. Therefore, an equally ordered very small gap and slot were observed because of the hollow cavity between the tungsten particles. It is believed that similar sized tungsten particles with spherical shape were coated on the glass substrate, which provided poor contact between the tungsten hollow spheres and FTO glass substrate. Fig. 14C illustrates GN–tungsten particles completely adhered to a glass substrate; a gap and slot were not observed between the particles layer and its substrate, which indicates a low

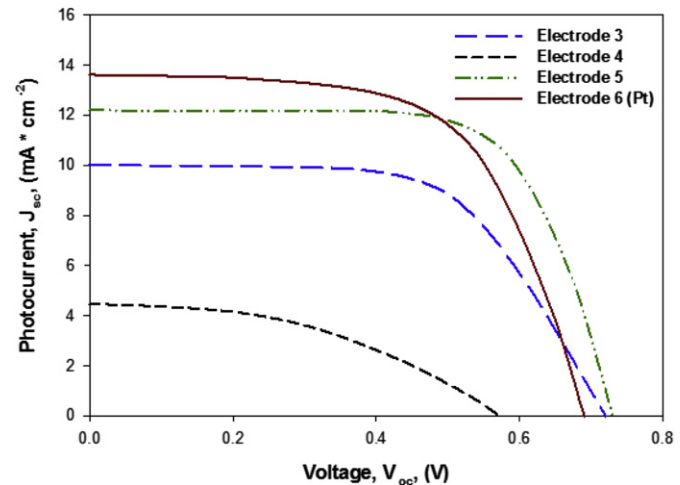


Fig. 15. The photocurrent–voltage (J – V) characteristics of DSSCs with GN, tungsten and GN–tungsten composite counter electrode structures.

resistance. This good adhesion of the GN–tungsten composite structure counter electrode occurred because when the GN and tungsten particles were mixed together, the tungsten nanoparticles possibly fully filled the slot of the GN particles to the substrate, which resulted in complete contact between the particle layer and substrate.

3.4. DSSC photovoltaic characteristics of the GN, tungsten and GN–tungsten composite counter electrode structures

To further improve the cell performance, GN structures incorporated with tungsten nanoparticles in ethanol solution by ultrasonication were used to prepare the counter electrode of DSSCs. The photovoltaic parameters of the cells were compared with that of a DSSC with a standard Pt counter electrode. The J – V curves and the corresponding photovoltaic parameters are shown in Fig. 15 and Table 3, respectively.

In the case of the DSSC with only a tungsten counter electrode, the observed J_{sc} , V_{oc} , FF and η were 4.48 mA cm^{-2} , 0.57 V and 0.41 , respectively, yielding an energy conversion efficiency of 1.06% . This poor photovoltaic performance can be ascribed to following aspects: (i) generally, tungsten alone has an insufficient electrochemical rate to reach the energy conversion efficiency. (ii) Fig. 14B shows poor adhesion of tungsten particles to a glass substrate, which causes a very slow electron transfer rate at the counter electrode and electrolyte interface and a reduced FF. Table 3 shows that the observed J_{sc} , V_{oc} , FF and η for the DSSC with GN–tungsten

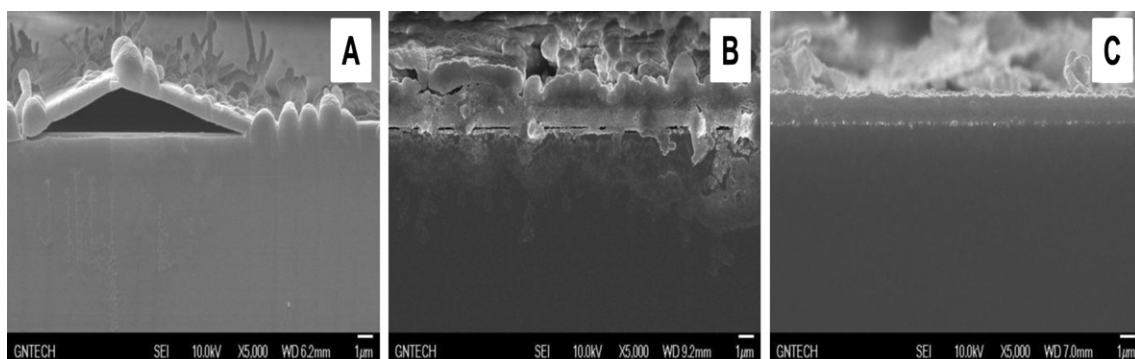


Fig. 14. Cross sectional SEM images of the (A) GN, (B) tungsten and (C) GN–tungsten composite counter electrodes.

Table 3

The photovoltaic parameters of DSSCs with GN, tungsten and GN–tungsten composite counter electrode structures.

Counter Electrode	J_{sc} (mA cm $^{-2}$)	V_{oc} (V)	FF	η (%)
Electrode 3	10.02	0.72	0.63	4.55
Electrode 4	4.48	0.57	0.41	1.06
Electrode 5	12.21	0.73	0.66	5.88
Electrode 6 (Pt)	13.62	0.69	0.63	5.92

composite counter electrode were 12.21 mA cm $^{-2}$, 0.73 V and 0.66, respectively, yielding an energy conversion efficiency of 5.88%. This excellent photovoltaic performance of DSSCs with GN–tungsten composite counter electrodes mainly arose from the following aspects: Firstly, the nanostructures of tungsten particles and the GN structure were dispersed uniformly and provided a large active surface area on the electrode (Fig. 11c), which benefited the transport of the liquid electrolyte [59]. Particularly, it is favourable to increase the I^-/I_3^- redox reaction rate on the counter electrode side, thus possibly enhancing the J_{sc} value [60]. Secondly, it was mentioned that increasing the surface area can also enhance the electrochemical activity, thus a higher electrochemical activity produced this slightly higher V_{oc} value (0.73 V). Finally, the excellent adhesion of the GN–tungsten composite to its substrate was supported by a low resistance at the interface between the electrolyte and the counter electrode for the I^-/I_3^- redox reaction, which increased the FF. For comparison, the corresponding values (J_{sc} , V_{oc} , FF and η) of the DSSCs with a Pt counter electrode were 13.62 mA cm $^{-2}$, 0.69 V, 0.63 and 5.92%, respectively. When compared to the Pt supported DSSC, despite the similar or higher V_{oc} and FF values, the DSSC with the GN–tungsten composite structure counter electrode showed a similar η value, owing to the smaller J_{sc} value. This very high J_{sc} value of DSSC with the standard Pt counter electrode was due to the quasi-transparent Pt counter electrode consisting of activated Pt nanoclusters on a glass substrate, which slightly reflected the unabsorbed portion of incident solar light towards the TiO₂ photoanode [33]. Then, the complex of the TiO₂ nanoparticles and ruthenium dye absorbed the reflected UV lights. Therefore, it is probable that an increased number of photoelectrons could be transferred within the DSSCs. Interestingly, because of the higher V_{oc} and FF values, the DSSC with GN–tungsten composite structure counter electrode showed a very similar photovoltaic efficiency to that of the DSSCs with standard Pt counter electrode. Finally, it is worth mentioning that the low cost GN–tungsten composite structure could be a potential material for replacing the conventional, expensive Pt in a DSSC.

4. Conclusion

In this study, graphene, tungsten and graphene–tungsten composite counter electrode structures were employed for Pt-free DSSC. The dispersibility of the GN structure in ethanol was improved by acid oxidation and planetary ball milling approaches, and the photovoltaic efficiency (4.55%) of the DSSC was also enhanced because of the high electrochemical activity, better adhesion of particles to the glass substrate and the improved specific surface area. The photovoltaic efficiency of DSSCs with the improved GN structure counter electrode was still lower than that of DSSCs with a standard Pt counter electrode. To further improve the cell performance, a GN structure incorporated with tungsten nanoparticles in ethanol was used as a counter electrode for a DSSC. Therefore, a DSSC that was fabricated with the GN–tungsten composite structure counter electrode achieved an overall photovoltaic efficiency of 5.88% under simulated AM 1.5 solar spectrum illumination at 100 mW cm $^{-2}$. This excellent photovoltaic

performance was very similar to that of a DSSC with a standard Pt counter electrode fabricated under the same conditions. It is worth mentioning that the low cost composite structure of GN–tungsten could be a potential material for replacing the conventional, expensive Pt in a DSSC.

Acknowledgement

This research was supported by Basic Science Research Program through the National Research Foundation of Korea (NRF) funded by the Ministry of Education, Science and Technology (No. 2012-008150) and the Future Leading Project through the Small and Medium Business Administration (No. S2044441).

References

- [1] H.J. Snaith, L. Schmidt-Mende, *Adv. Mater.* 19 (2007) 3187–3200.
- [2] B. O'Regan, M. Grätzel, *Nature* 353 (1991) 737–740.
- [3] N.L. Yang, J. Zhai, D. Wang, Y.S. Chen, L. Jiang, *ACS Nano* 4 (2010) 887–894.
- [4] T. Stergiopoulos, I.M. Arabatzis, G. Katsaros, P. Falaras, *Nano Lett.* 2 (2002) 1259–1261.
- [5] L.M. Peter, *Phys. Chem. Chem. Phys.* 9 (2007) 2630–2642.
- [6] T.N. Murakami, M. Grätzel, *Inorganica Chim. Acta* 361 (2008) 572–580.
- [7] E. Olsen, G. Hagen, S.E. Lindquist, *Sol. Energy Mater. Sol. Cells* 63 (2000) 267–273.
- [8] K. Imoto, K. Takahashi, T. Yamaguchi, T. Komura, J.I. Nakamura, K. Murata, *Sol. Energy Mater. Sol. Cells* 79 (2003) 459–469.
- [9] T.N. Murakami, S. Ito, Q. Wang, M.K. Nazeeruddin, T. Bessho, I. Cesar, P. Liska, R.H. Baker, P. Comte, P. Pechy, M. Grätzel, *J. Electrochem. Soc.* 153 (2006) A2255–A2261.
- [10] G. Veerappan, K. Bojan, S.W. Rhee, *ACS Appl. Mater. Interfaces* 3 (2011) 857–862.
- [11] X. Mei, S.J. Cho, B. Fan, J. Ouyang, *Nanotechnology* 21 (2010) 395202.
- [12] J.K. Han, H.J. Kim, D.Y. Kim, S.M. Jo, S.Y. Jang, *ACS Nano* 4 (2010) 3503–3509.
- [13] H. Zheng, C.Y. Neo, X. Mei, J. Qiu, J. Ouyang, *J. Mater. Chem.* 22 (2012) 14465–14474.
- [14] L. Kavan, J.H. Yum, M. Grätzel, *ACS Nano* 5 (2011) 165–172.
- [15] K.S. Novoselov, A.K. Geim, S.V. Morozov, D. Jiang, Y. Zhang, S.V. Dubonos, I.V. Grigorieva, A.A. Firsov, *Science* 306 (2004) 666–669.
- [16] Y.B. Tang, C.S. Lee, J. Xu, Z.T. Liu, Z.H. Chen, Z. He, Y.L. Cao, G. Yuan, H. Song, L. Chen, L. Luo, H.M. Cheng, W.J. Zhang, I. Bello, S.T. Lee, *ACS Nano* 4 (2010) 3482–3488.
- [17] S. Sun, L. Gao, Y. Liu, *Appl. Phys. Lett.* 96 (2010) 083113–083115.
- [18] J.D. Roy-Mayhew, D.J. Bozyn, C. Punckt, I.A. Aksay, *ACS Nano* 4 (2010) 6203–6211.
- [19] A.K. Geim, K.S. Novoselov, *Nat. Mater.* 6 (2007) 183–191.
- [20] A.K. Geim, P. Kim, *Sci. Am.* 298 (2008) 90–97.
- [21] E.J. Yoo, J. Kim, E. Hosono, H.S. Zhou, T. Kudo, I. Honma, *Nano Lett.* 8 (2008) 2277–2282.
- [22] M.D. Stoller, S. Park, Z. Yanwu, J. An, R.S. Ruoff, *Nano Lett.* 8 (2008) 3498–3502.
- [23] B. Munkhbayar, Md. J. Nine, Jinseong Jeoun, Munkhjargal Bat-Erdene, Hanshik Chung, Hyomin Jeong, *Powder Technol.* 234 (2013) 132–140.
- [24] P.K. Shen, S. Yin, Z. Li, C. Chen, *Electrochim. Acta* 55 (2010) 7969–7974.
- [25] E.C. Weigert, A.L. Stottlemeyer, M.B. Zellner, J.G. Chen, *J. Phys. Chem. C* 111 (2007) 14617–14620.
- [26] Y. Hara, N. Minami, H. Itagaki, *Appl. Catal. A* 323 (2007) 86–93.
- [27] Y. Gao, L. Chu, M. Wu, L. Wang, W. Guo, T. Ma, *J. Photochem. Photobiol. A Chem.* 245 (2012) 66–71.
- [28] A.R. Ko, J.K. Oh, Y.W. Lee, S.B. Han, K.W. Park, *Mater. Lett.* 65 (2011) 2220–2223.
- [29] Y. Saito, S. Uchida, T. Kubo, H. Segawa, *Thin Solid Films* 518 (2010) 3033–3036.
- [30] K. Hara, Z.G. Zhao, Y. Cui, M. Miyauchi, M. Miyashita, S. Mori, *Langmuir* 27 (2011) 12730–12736.
- [31] E. Kymakis, M.M. Stylianakis, S.D. George, E. Stratakis, E. Koudoumas, C. Fotakis, *Sol. Energy Mater. Sol. Cells* 96 (2012) 298–301.
- [32] M.Y. Yen, M.C. Hsiao, S.H. Liao, P.I. Liu, H.M. Tsai, C.C.M. Ma, N.W. Pu, M.D. Ger, *Carbon* 49 (2011) 3597–3606.
- [33] B. Munkhbayar, S. Hwang, J. Kim, K. Bae, M. Ji, H. Chung, H. Jeong, *Electrochim. Acta* 80 (2012) 100–107.
- [34] D.W. Zhang, X.D. Li, H.B. Li, S. Chen, Z. Sun, X.J. Yin, S.M. Huang, *Carbon* 49 (2011) 5382–5388.
- [35] S.D. Kim, J.W. Kim, J.S. Im, Y.H. Kim, Y.S. Lee, *J. Flour. Chem.* 128 (2007) 60–64.
- [36] A.C. Ferrari, J. Robertson, *Phys. Rev. B* 61 (2000) 14095–14107.
- [37] J. Shen, M. Shi, B. Yan, H. Ma, N. Li, Y. Hu, M. Ye, *Colloids Surf. B* 81 (2010) 434–438.
- [38] K.N. Kudin, B. Ozbas, H.C. Schniepp, R.K. Prud'homme, I.A. Aksay, R. Car, *Nano Lett.* 8 (2008) 36–41.

- [39] P. Hasin, M.A. Alpuche-Aviles, Y. Wu, *J. Phys. Chem. C* 114 (2010) 15857–15861.
- [40] J.H. Lee, K.Y. Rhee, S.J. Park, *Int. J. Hydrogen Energy* 35 (2010) 7850–7857.
- [41] Z. Li, Y. Chen, Y. Du, X. Wang, P. Yang, J. Zheng, *Int. J. Hydrogen Energy* 37 (2012) 4880–4888.
- [42] M. Li, S. Xu, M. Tang, L. Liu, F. Gao, Y. Wang, *Electrochim. Acta* 56 (2011) 1144–1149.
- [43] B. Munkhbayar, Md. J. Nine, S. Hwang, J. Kim, K. Bae, H. Chung, H. Jeong, *Chem. Eng. Process.* 61 (2012) 36–41.
- [44] D.W. Zhang, X.D. Li, S. Chen, F. Tao, Z. Sun, X.J. Yin, S.M. Huang, *J. Solid State Electrochem.* 14 (2010) 1541–1546.
- [45] J. Luo, H.J. Niu, W.J. Wu, C. Wang, X.D. Bai, W. Wang, *Solid State Sci.* 14 (2012) 145–149.
- [46] H. Sakane, T. Mitsui, H. Tanida, I. Watanabe, *J. Synchrotron Radiat.* 8 (2001) 674–676.
- [47] T.S. Ong, H. Yang, *Carbon* 38 (2000) 2077–2085.
- [48] H.Q. Li, Y.G. Wang, C.X. Wang, Y.Y. Xia, *J. Power Sources* 185 (2008) 1557–1662.
- [49] C.Y. Liu, K.C. Huang, P.H. Chung, C.C. Wang, C.Y. Chen, R. Vittal, C.G. Wu, W.Y. Chiu, K.C. Ho, *J. Power Sources* 217 (2012) 152–157.
- [50] L.H. Chang, C.K. Hsieh, M.C. Hsiao, J.C. Chiang, P.I. Liu, K.K. Ho, C.C.M. Ma, M.Y. Yen, M.C. Tsai, C.H. Tsai, *J. Power Sources* 222 (2013) 518–525.
- [51] J. Yu, J. Fan, B. Cheng, *J. Power Sources* 196 (2011) 7891–7898.
- [52] J. Fan, S. Liu, J. Yu, *J. Mater. Chem.* 22 (2012) 17027–17036.
- [53] Q. Xiang, J. Yu, M. Jaroniec, *Chem. Soc. Rev.* 41 (2012) 782–796.
- [54] Q. Xiang, J. Yu, M. Jaroniec, *J. Am. Chem. Soc.* 134 (2012) 6575–6578.
- [55] J. Zhang, J. Yu, M. Jaroniec, J.R. Gong, *Nano Lett.* 12 (2012) 4584–4589.
- [56] G. Wang, X. Shen, J. Yao, J. Park, *Carbon* 47 (2009) 2049–2053.
- [57] S. Pal, C. Jacob, *Appl. Surf. Sci.* 253 (2007) 3317–3325.
- [58] B. Tan, Y.Y. Wu, *J. Phys. Chem. B* 110 (2006) 15932–15938.
- [59] Y. Saito, W. Kubo, T. Kitamura, Y. Wada, S. Yanagida, *J. Photochem. Photobiol. A Chem.* 164 (2004) 153–157.
- [60] S.S. Jeon, C. Kim, J. Ko, S.S. Im, *J. Phys. Chem. C* 115 (2011) 22035–22039.